

# Magnetostatic Spin Waves and Magnetic-Wave Chaos in Ferromagnetic Films.

## II. Numerical Simulations of Non-Linear Waves

Yu.E. Kuzovlev, Yu.V. Medvedev, and N.I. Mezin\*

*A.A.Galkin Physics and Technology Institute of NASU,*

*ul. R.Luxemburg 72, 83114 Donetsk, Ukraine*

### Abstract

A method and some results of numeric simulations of magnetostatic spin waves in ferromagnetic films are expounded, in comparison with the theory earlier presented in arXiv preprint 1204.0200. In particular, roles of films finiteness (edges) and defects in formation of linear and non-linear magnetostatic wave patterns, excitation and evolution of two-dimensional solitons, and chaotic non-linear ferromagnetic resonance are considered.

PACS numbers: 75.30.Ds, 75.40.Mg, 76.50.+g

---

\*Electronic address: kuzovlev@fti.dn.ua

## Introduction

This preprint represents first, preparatory, stage of numerical investigation of magnetostatic spin waves' chaos in ferrite films realized between 2001 and 2003 under particular support of Multimanetic Solutions Ltd. Its main contents will be submitted in separate preprint, as Part III of the manuscript whose Part I was devoted to theory of magnetostatic waves and already presented by our arXiv preprint 1204.0200.

Our primary purposes here, in Part II, and in the next Part III were: (i) to test numeric algorithms based on spatial discretization of film's volume; (ii) to estimate an extent to what the theory developed for idealized infinite films is applicable to real finite-size (and may be defective) films; (iii) to examine theoretical concepts, - e.g. "quasi-local magnetic energy density" (see below), - which have no unambiguous theoretical definition (because of strong non-locality of dipole interactions or by other reasons) but can be useful for description of non-linear magnetic-wave phenomena; (iv) to visually indicate mechanisms and forms of magnetostatic-wave chaos, (v) to see what of them are most appropriate for practical use, and numerically investigate possibilities of control and synchronization of this chaos.

## 6. NUMERICAL METHODS AND NUMERICAL SIMULATIONS OF EXTERNALLY DRIVEN FILMS

The modern theory of nonlinear wave processes in ferromagnets and ferrites is not developed to an extent sufficient for fruitful applications to so complex phenomenon as magnetic chaos. By this reason, numerical simulations must be in anyway useful, since they

(i) serve as powerful "microscope" to watch for magnetization dynamics at its natural temporal scales, from the one tenth part of nanosecond up to tens microseconds, and in this way allow to

- (ii) verify existing theoretical models, find prompts for improving analytical theory, and
- (iii) obtain concrete practically acceptable estimates, conclusions and predictions.

Although many aspects on nonlinear wave dynamics may be modelled in terms of popular NSE (nonlinear Schrödinger equation, see Sec.5), it does not approach for above purposes, because it contains no natural amplitude limit for waves and solitons. Indeed, in Eq.11 itself and in its solitonic solutions (5.25) and (5.26) the amplitudes,  $|\Psi|$  and  $A$ , may be

arbitrary large, while physically, according to relations (5.9), they can not exceed a level of order of unit. This means that at certain critical time moments of chaotic dynamics other higher-order non-linearities play significant role. Besides, NSE neglects odd powers of non-linearity and related parametric processes.

Therefore, numerical simulation algorithms should be based on complete Landau-Lifshitz-Gilbert equation (2.1). At this approach, trivial normalization of spin length to unit ensures taking into account all orders of non-linearity.

### 6.1. NUMERICAL ALGORITHM.

To solve Eq.2.1, the classical third-order Runge-Kutta algorithm was used, in its adaptive version with time step being automatically chosen as large as possible at fixed precision. Nevertheless, running of Eq.2.1 appears not a fast procedure. The matter is that non-local dipole interaction should be calculated by means of Fourier transform, which even in its most fast form takes much greater time than, say, calculation of gradients and Laplacians.

Moreover, if the transform was located within the sample volume then the non-local interaction would be represented by a function of two spatial points,  $r_1$  and  $r_2$  instead of only their difference  $r_1 - r_2$ , and Fourier transform could not be applied. Therefore, when discretizing the sample volume into  $N_x \times N_y \times N_z$  cells ("spins"), it is necessary to consider at least  $N'_x \times N'_y \times N'_z$  cells, - with  $N'_{x,y,z} \geq 2N_{x,y,z} - 1$ , - in order to correctly represent the dipole interaction kernel in the  $(r_1 - r_2)$ -space (fortunately,  $N'_{x,y,z} = 2N_{x,y,z} - 1$  or  $N'_{x,y,z} = 2N_{x,y,z}$  are always sufficient numbers). The award for this complication is that all the finite-size and boundary effects are taken into account.

The algorithm was tested by modeling magnetization of small ferromagnetic slabs, with sizes of order of tens  $r_0$  (exchange interaction radius). It was possible to observe (i) formation of magnetic vortices and domains at sufficiently weak field, (ii) their death at moderate fields, with residual demagnetization at former domain boundaries, (iii) almost uniform magnetization at strong fields with significant demagnetization at sample boundaries only, (iv) hysteretic effects, characteristic hysteresis curves on  $H - B$  -plane, re-magnetization chaos and noise at periodically varying field (chaotic hysteresis).

### 6.2. CONCRETIZATION OF NUMERICAL TASKS.

We will be most interested in comparatively large-scale phenomena in YIG films whose typical size is about  $7 \text{ mm} \times 2 \text{ mm} \times 10 \text{ micron}$ . Besides, we want to apply such kind of film magnetization which ensures maximum MW frequencies at minimum value of

magnetizing external field  $H_0$  . This requirement is satisfied if (i) film is tangentially magnetized and (ii) the surface magnetostatic waves (MSW) are explored which propagate perpendicularly to static magnetization (see Secs.3-4). Practically suitable wave length,  $\lambda$  , of these MSW lies in the interval  $0.1 \div 1$  mm , that is  $\lambda/D \gtrsim 10$  (  $D$  is film thickness), while suitable cross sizes of MSW inductors (antennas) are comparable with  $D$  .

### 6.3. ASSUMPTIONS AND SIMPLIFICATIONS.

If we took the  $r_0$  (exchange radius  $\sim 5 \cdot 10^{-6}$  cm) be the scale of spatial discretization, then (at above mentioned film sizes)  $N_x \times N_y \times N_z$  would be  $\sim 10^{12}$  . Hence, literal simulation of real samples is impossible.

The natural possibility to simplify numerical problems arises from the fact that surface MSW with  $\lambda/D \gtrsim 10$  are almost uniform across film's thickness (i.e. in  $z$  -direction). Therefore, we can use the averaging over thickness. Then the latter becomes basic spatial scale, and we come to two-dimensional discretization lattice, with  $N_z = 1$  and  $N_x \times N_y$  determined by the film length to thickness and wide to thickness ratios.

In this approach, we inevitably neglect bulk MSW modes with  $N > 0$  which are essentially non-uniform in respect to thickness (see Part I, Sec.4). These non-uniform bulk waves are not directly excitable by thick antennae, but they can be generated from surface MSW by means of nonlinear fourth-order G-P-processes or third-order P-processes (Sec.5) and thus influence their dynamics. Nevertheless, our formally crucial simplification has physical grounds as follow.

In fact, there are similar fourth-order interactions between surface MSW themselves. We can suppose that just these interactions are dominating in surface MSW dynamics because realize in resonant way, while interaction with most of non-uniform bulk modes is far from resonances. Indeed, their frequencies lie below uniform precession frequency,  $\omega_u$  , while frequencies of surface MSW are higher than  $\omega_u$  . If comparing the dispersion law (3.38) for DE-waves and Eqs.4.28 and 4.29 for dispersion of bulk modes, one can verify that their frequencies are close at

$$q_{N\pm} \approx \frac{\pi N}{D} \sim \frac{2\pi}{r_0} \sqrt{\frac{2\pi D}{(H_0 + 2\pi)\lambda}} \sim 1.5 \cdot 10^5 \text{ cm}^{-1}, \quad N \sim 40, \quad (1)$$

only. In reality, so short-wave modes must be damped certainly stronger than long surface waves. At the same time, the latter effectively influence one upon another around (in  $k$  -

space) equi-frequency curves (shown in Fig.4a, see Sec.4). By these reasons, we expect that fourth-order interaction with non-uniform modes is relatively insignificant. The same can be argued in respect to third-order parametric by surface waves (all the more, at  $\omega_u/2 < \omega_1$ , i.e. at  $H_0 \gtrsim 4\pi/3$ , this process is forbidden at all).

At present this is (i.e. was ten years ago) unavoidable simplification, since at  $N_z \gtrsim 2N$ , that is at  $N_z \gtrsim 80$ , again numerical simulation would be unrealistic even with Pentium-IV in our order. Rigorous analysis of role of non-uniform (multi-layered) MW in nonlinear long-wave dynamics is the interesting task for future. Now, we yet are forced to deal with numerical model rather than with literal numerical simulation.

#### 6.4. NUMERICAL STRATEGY.

After the simplification, film thickness takes the role of length unit. Moreover, the size of discretization lattice, in units of  $D$ , can be chosen  $n \times n \times 1$ , which allows to simulate the film area  $nN_x D \times nN_y D$ . The permissible additional roughening,  $n$ , depends on characteristic minimum wave length in a situation under analysis. To speed up calculations, we may choose a greater  $n$  but then lower it if necessary.

In fact, the values  $1 \leq n \leq 8$ ,  $20 \leq N_y \leq 170$ , and  $70 \leq N_x \leq 256$  were used [ten years ago, while now it is possible to take greater  $N_x$ ,  $N_y$  and simultaneously  $N_z > 1$ , i.e. fractional  $n$ ]. Of course, the dipole interaction of discrete cells (effective spins) was calculated with taking into account their shape as determined by  $n$ . A choice of definite “magic”  $N_x$  and  $N_y$  numbers ensured most fast FFT on a  $N'_x \times N'_y$  lattice (with  $N'_{x,y} \geq 2N_{x,y} - 1$ ). Nevertheless, typically from 1 to 5 real time seconds were elapsed per one period of spin precession,  $\sim 0.3$  ns, since several FFT’s and inverse FFT’s should be performed at each time step.

At given uniform magnetizing field  $H_0$ , firstly static magnetization pattern was calculated and conserved in memory, then serving as initial ground state for wave and soliton structures caused by time-varying currents.

The anisotropy is what can be simply taken into account with no numerical problems. But it evolves several parameters at once. At present stage, we want to obtain numerical “reference point data” with minimum amount of free parameters and therefore intentionally omit anisotropy.

#### 6.5. NUMERICAL FRICTION.

It is well known that the time discretization when numerically solving differential dynamic

equations inevitably results in more or less effective friction (or may be negative one). In our case this artifact also takes place leading to energy relaxation even if the friction coefficient is put on be zero,  $\gamma = 0$ . Interestingly, this excess numerical relaxation excellently obeys exponential law and therefore works as increase of  $\gamma$ ,  $\gamma \rightarrow \gamma_{eff} = \gamma + \gamma_{num}$ .

The value of  $\gamma_{num}$  depends on mean time step. Typically, the latter was between one thirtieth and one twentieth part of the precession period resulting in  $\gamma_{num} \approx 0.0004$ . This friction is just suitable to simulate good but not best samples. However, it could be made lower than 0.0001 if decrease mean time step to about one fortieth part of the period. Below, the designation  $\gamma$  will stand for  $\gamma_{eff}$ .

## 6.6. MSW EXCITATION BY WIRES AND LOOPS.

First of all, excitation of weak magnetic waves in small-area film by wire and loop inductors was numerically watched for. At present, we confined ourselves by inductors with round cross-section and radius greater than  $D$ , oriented along  $y$ -axis in parallel to magnetizing field. Corresponding current induced field,  $h(r, t) = \{h_x(x, y, t), 0, h_z(x, y, t)\}$ , was calculated from usual magnetostatics formulas. For relations between physical and dimensionless time and frequency units, see Sec.3.

Examples of such the simulations are illustrated by Figs.6a-c. Two rather obvious conclusions do follow from these pictures.

(i) At given microwave frequency of linear wire or loop current, not a single plane wave is induced (as it would be in infinite-size film), but a spectrum of waves with different length, including ones with non-zero  $y$ -component of wave vector (notice that at  $H_0 = 3$  the uniform precession frequency  $\omega_u \approx 6.83$ ). In fact, in Fig.6a and Fig.6b we observe eigen-modes (or compositions of nearly degenerated eigen-modes) of small (finite-size) film. Comparison of these figures shows that, naturally, loop inductor ensures better wave selection and simpler magnetization pattern.

(ii) At the same time, the spatial Fourier spectrum of excited pattern can be intelligently interpreted in terms of infinite film theory (Sec.4), as illustrated by contour plot in Fig.6b. In this plot, a number of lines surrounding some point of  $k$ -plane indicates its contribution to summary picture. Clearly, spectrum maxima well agree with equi-frequency curves in  $k$ -plane of infinite film (Fig.4a in Sec.4), in spite of not large film length to wavelength ratio ( $\approx 5$ ). Hence, so visible characteristic rhombic structures in Figs.6a-b directly reflect characteristic slopes of equi-frequency curve responding to the excitation frequency.

The Fig.6c justifies that particular eigen-modes and eigenfrequencies of even small-size film may be quantitatively close to waves in infinite film. One particular mode is selected by equating pump frequency to that of plane surface (Damon-Eshbach) wave with  $k_x = \pm 2\pi/2l$  and  $k_y = 0$  which would be generated by the same loop in infinite film. We see that result is almost plane wave too, i.e. indeed resonance takes place. Nevertheless, this mode contains some contribution from plane waves with  $k_x \approx \pm 3 \cdot 2\pi/2l$  and  $k_y \neq 0$  which possess the same eigenfrequency and occur resonantly excitable by the same loop.

### 6.7. ROLE OF FILM EDGES.

In the top of Fig.7, static distributions of the internal field,  $W_0$ , and magnetization in small-area film are shown, at moderate value of external field,  $H_0 = 3M_s$ . Clearly, in most part of the film practically uniform magnetization realizes, with  $W_0 \approx H_0$ . Substantial demagnetization takes place at narrow strips only which adjoin film edges perpendicular to external field and have width  $\sim D$  (as it was stated in Sec.3).

Since the internal field is lowered at these demagnetized strips, a local spin precession frequency there also is lowered. Therefore, usually these strips take almost none part in shaping and propagation of waves, as if spins were partially pinned there. These statement can be illustrated by Figs.6a-c.

In principle, specific edge waves can be excited in the demagnetized regions. However, this is rather exotic phenomenon, and it was not a case in practically all of our numerical simulations.

### 6.8. A SOLITON FED UP BY WEAK CONSTANT PARAMETRIC PUMP.

One more exotic phenomenon is illustrated at bottom of Fig.7, concretely, very small-amplitude soliton (spatially localized wave packet) created and then supported by extremely weak parametric pump. The loop current parallel to external field (i.e. to  $y$ -axis) induces field with amplitude of its  $x$ -component  $\sim 10^{-4}$  (i.e.  $\sim 0.01$  Oe in real units) and frequency  $\omega_e = 14.5$  which is far out off total MSW frequency band (with upper bound  $= H_0 + 2\pi \approx 9.3$ , see Sec.4). As the result, long weak envelope soliton is formed whose carrying frequency equals to half of  $\omega_e$ , with magnitude  $\|S_{\perp x}\| \sim 10^{-5}$  and width  $\sim 150D$  (at film length  $= 432D$ ). Interestingly, the two latter quantities approximately satisfy the relation between amplitude and width of bright solitons which follows from Eqs.5.15 and 5.25. Although bright solitons moving perpendicular to external field are formally forbidden in infinite film, this simulation shows that similar objects are

permitted for finite-size film. Besides, we detect that parametric excitation allows to create small-amplitude soliton avoiding the restriction (5.23).

Further behavior of this object is even more intriguing. It oscillates between film ends (see Fig.7) undergoing some decay after reflection from the distant end but more or less amplification while reflecting from the edge where inductor takes place. The dot line separates period of strong amplification of the soliton due to occasionally “good” relation between phases of its carrier and pump. Dimensionless time and frequency in Fig.7 are real ones as expressed in units of  $\tau_0$  and  $f_0$ , respectively (see Sec.2 and 3).

From the point of view of Eq.5.1 the parametric process under discussion must be described by quadratic term  $\langle S_0, h \rangle [S_0, S_\perp]$  in second row. Interestingly, in view of  $h_y = 0$  we should conclude that pump,  $\langle S_0, h \rangle$ , mostly acts at the demagnetized edges. Among our numerical collection, this is exclusive example when film edges play a key role.

Below, we will deal with non-parametric pump whose frequency belongs to the MSW band. Like here, in all forthcoming examples inductors are parallel to external magnetizing field.

#### 6.9. CREATION OF SOLITONS BY NON-PARAMETRIC PULSE PUMP.

The Fig.8a shows the consequence of intensive radio-impulse of current passed through wire inductor at one of ends of relatively large-area film. The impulse duration was about twenty periods of the carry frequency,  $\omega_e = 7.5$ . At a distance from the inductor, the induced magnetization precession impulse is deformed. If its initial amplitude was sufficiently large then further it breaks into a chain of pulses with almost zero dips between highest of them. The picture in Fig.8a can be qualified as formation of gray solitons inside finite-length wave packet.

The critical breaking level of amplitude is just its maximum after breaking, in this example  $\|S_{\perp x}\| \approx 0.15$ . This observation is in reasonable agreement with the estimate of this level which follows from Eqs.5.9, 5.10 and 5.23,

$$\|S_{\perp x}\| \approx A_{\min} \sqrt{p} = \sqrt{\Gamma p / |\varkappa|} \approx 0.1 \quad (2)$$

(at friction  $\gamma = 0.0005$  what took place). In all the below discussed numerical simulations, close threshold values,  $0.1 \lesssim \|S_{\perp x}\| \lesssim 0.2$ , mark transition to brightly expressed non-linear effects and to magnetic chaos.

#### 6.10. CHAOS UNDER UNIFORM RESONANT MICROWAVE FIELD.



In most of previously reported experiments on magnetic chaos, the latter was excited by nearly uniform microwave magnetic field,  $h(r, t)$ , either using parallel parametrical pump when  $h \parallel S_0$  and excitation frequency  $\omega_e \sim 2\omega_u$  or through perpendicular ferromagnetic resonance (FMR) when  $h \perp S_0$  and  $\omega_e \sim \omega_u$ . Consider the second variant since it is more close to chaotic auto-generation of MSW to be under our interest.

The Fig.8b demonstrates modeling of nonlinear FMR in moderate-area film at  $H_0 = 3$  and  $\gamma = 0.0007$ , under uniform microwave field parallel to  $x$ -axis. Due to finite-size effects (edge demagnetization), factual (numerically found) uniform precession frequency,  $\omega_u \approx 6.785$  (at  $H_0 = 3$ ), is slightly lower then theoretical value for infinite film,  $\omega_{u\infty} \approx 6.83$ . Taking  $\omega_e$  sufficiently close to  $\omega_u$ , it is possible to obtain strong response to weak perpendicular field  $h \sim 0.001M_s \sim 0.1$  Oe. Naturally, the response is indicated by amplitude of uniform component of  $S_\perp$ , i.e.  $\langle S_\perp \rangle \equiv \int_V S_\perp dr / V$  where  $V$  stands for film volume.

After sharp two times increase of pump we observe increase of  $\langle S_\perp \rangle$ 's amplitude which monotonically tends to nearly two times larger value. However, next increases of  $h$  by the same step result in smaller and non-monotone response. At  $h = 0.007$ , the response transforms into periodic oscillations. At last, when  $h = 0.008$ , these oscillations turn into chaotic one, at time moment marked as "burst" on Fig.8b. More careful repetition of this process (with smaller step) allows to notice at least one or two period-doubling bifurcations of regular oscillations (as well know in theory of dissipative chaos [1]).

Interestingly, to reach the chaos, well satisfied resonance condition  $\omega_e \approx \omega_u$  is quite necessary. For instance, at  $\omega_e = \omega_{u\infty}$  (i.e. at frequency deviation less than 1%) the only result of even very intensive pump,  $h \sim 1$ , is strongly nonlinear but regularly oscillating long-wave structure.

Other characteristic observation is the hysteresis of chaos: if  $h$  is lowered from 0.008 than chaotic regime remains at least down to  $h = 0.005$ .

### 6.11. SHORT-WAVE EXPLOSION AND TRANSITION TO CHAOS.

Usually, experimental magnetic chaos is analyzed in terms of particular wave modes, that is in momentum space (see, for instance, [2,3]). In our simulation, we can view also how it looks in real space, and watch for spatial-temporal picture of transition from regular motion to chaos. Characteristic scenario of this transition is illustrated in Fig.9.

When FMR is still regular, rather smooth magnetization pattern takes place with one or

three maximums of oscillations and precise mirror symmetry (with respect to middle lines of rectangular film area). However, the closer is the transition the higher and narrower is the central maximum. This means that spectrum of excited MSW becomes more and more wide, but still coherent, in the sense that all the waves are mutually connected by some rigid phase relations. At critical “burst” time moment the central maximum collapses into peak very narrow in  $x$ -direction and rather flat (elongated) in  $y$ -direction (i.e. along static magnetization). Then this peak blows up giving freedom to the short waves. The latter incoherently scatter in all the directions in their turn giving rise to complicated (chaotic) magnetization pattern. Beginning of this unstable explosive stage is shown at bottom of Fig.9. Notice that corresponding magnitude of  $S_{\perp x}$  confirms estimate (2).

Important sign of transition to chaos is violation of the mirror symmetry. The symmetry with respect to  $180^\circ$  rotation only remains after the explosion. Clearly, this symmetry is invoked by that of the static  $S_0$  pattern (see Fig.7).

At later time, most short of the explosively induced waves decay. In further stationary chaotic regime, magnetization picture more or less restores both smoothness and mirror symmetry. But, naturally, increase of pump rises both short-wave contents and asymmetry. Moreover, under sufficiently intensive pump new similar explosions (bursts) are repeated from time to time, serving as “discharges” of excessive energy accumulated by long waves. This may be called strong chaos.

#### 6.12. EXCESS ENERGY AND POWER ABSORPTION.

The top of Fig.9 demonstrates typical chaotic behavior of excess film energy,  $E$ , and of power absorption by film,  $P$ , both related to unit volume (discretization cell). Here and below, “excess energy” (or simply “energy”) will term increase of magnetic energy due to the excitation,  $S_{\perp}$ , but excluding direct  $S_{\perp}$ ’s interaction with pump field (i.e. except  $-\int \langle h, S_{\perp} \rangle dr / V$ , see Sec.2). The power absorption,  $P$ , describes energy flow into film which is spent for both  $E$  and dissipation in the film interior. Hence, in general

$$\frac{dE}{dt} = P - P_{dis}, \quad P = \left\langle \int \left\langle h(r, t), \frac{dS_{\perp}}{dt} \right\rangle \frac{dr}{V} \right\rangle_T, \quad (3)$$

with  $P_{dis}$  being dissipated power per unit volume. Symbol  $\langle \rangle_T$  designates time averaging with respect to spin precession. These equations directly follow from the basic Eq.2.1.

It is natural to expect that

$$P_{dis} \approx 2\Gamma(E - E_0) , \quad (4)$$

at some  $E_0$  , and  $\Gamma$  being previously considered dissipation rate of magnetization. At  $\gamma = 0.0007$  first of Eqs.5.10 gives  $2\Gamma \approx 0.013$  , then energy relaxation time is  $\sim 1/2\Gamma \approx 80$  . Indeed, approximately such the time scale can be viewed at plot (A) in Fig.9. Further, let us put on  $\langle S_{\perp x} \rangle = \|S_x\| \sin[\omega_e t - \phi]$  where  $\|S_x\|$  and  $\phi$  designate amplitude and phase, respectively, of the uniform component of spin precession. Then

$$P = h \left\langle \sin(\omega_e t) \frac{d\langle S_{\perp x} \rangle}{dt} \right\rangle_T \approx \frac{1}{2} \omega_e h \|S_x\| \sin \phi \quad (5)$$

At  $\|S_x\| \approx 0.1$  (as prompted by Fig.8b),  $h = 0.008$  and  $\phi \approx \pi/2$  (which means good resonance) this relation results in  $P \sim 2.5 \cdot 10^{-3}$  , in agreement with plot (B) in Fig.9. Hence, rough average characteristics of chaotic variables are easy explainable.

Much harder task is to explain chaotic deviations from average values. For instance, in plots (A) and (B) energy and power nearly follow one another. It is clear: the energy comes from power absorption, but the latter depends on the phase  $\phi$  which in its turn must be sensitive to energy, because of non-isochronity of spin precession (see Sec.5). But without an adequate dynamical model for this connection we can not estimate details of chaotic time series.

### 6.13. INSTANT FREQUENCY.

Directly, our numerical algorithm produces fast oscillating time series. To extract from them relatively slow time-varying (“instant”) amplitudes and phases (like  $\|S_x\|$  and  $\phi$  above), and corresponding instant frequencies (e.g.  $\omega_e - d\phi/dt$  ), there are two ways. One is to build analytical signals by means of (discrete) Gilbert transformation. Another way is to indicate maximums, minimums and zero-crossings of oscillating variable. If  $t_n$  ,  $n = \dots, -1, 0, 1, \dots$  , are estimates of time moments when zero-crossing does occur, then instant frequency at  $t \approx t_n$  can be determined as  $\omega_{in} = 2k\pi/(t_{n+k} - t_{n-k})$  , where  $k \geq 1$  .

If disposing this quantity, the phase can be restored by discrete numerical integration. This method is more comfortable and fast than Hilbert transformation, but ensures not worse (usually better) accuracy what was confirmed by special tests.

### 6.14. QUASI-LOCAL ENERGY DENSITY.

Because of relations (2.9) and (4.1), the excess energy (per unit volume) can be represented in the form

$$E = E_{loc} + E_{nonloc} , \quad E_{loc} = \int e_{loc} \frac{dr}{V} , \quad e_{loc} \equiv H_0(1 - S_y) + 2\pi S_z^2 \quad (6)$$

Here  $E_{nonloc}$  is contribution from non-local (non-singular) part of dipole interaction in plate geometry (Sec.4), while  $E_{loc}$  consists of its local (singular) part and also local first term of Eq.2.9.

For uniform precession (even let large-amplitude and strongly non-linear),  $E_{nonloc}$  vanishes, hence, the sum  $e_{loc} - \langle h(t), S \rangle$  plays the role of Hamiltonian of the average spin. In particular, in autonomous regime of uniform precession, at  $h = 0$ ,  $e_{loc}$  becomes integral of motion.

Importantly,  $E_{nonloc}$  may be negligible as compared with  $E_{loc}$  in non-uniform chaotic case too. Indeed, according to equations (4.1-2), (4.6) and (6), the non-local contribution can be estimated as

$$E_{nonloc} \approx \pi D \int \left( \frac{k_x^2}{|k|} |\tilde{S}_x(k)|^2 - |k| |\tilde{S}_z(k)|^2 \right) dk , \quad (7)$$

$$\left| \frac{E_{nonloc}}{E_{loc}} \right| \lesssim \frac{\pi D \langle |k| \rangle}{H_0} , \quad \langle |k| \rangle \equiv \int |k| |\tilde{S}_x(k)|^2 dk \left( \int |\tilde{S}_x(k)|^2 dk \right)^{-1} ,$$

with  $\tilde{S}_{x,z}(k)$  denoting spatial Fourier transform of magnetization. If long MSW (with  $D|k| \ll 1$ ) are dominating in magnetization pattern, then the excess energy is well characterizable by  $E_{loc}$ . As the consequence, the quantity  $e_{loc}$  behaves like local integral of motion and thus can be termed quasi-local energy density.

#### 6.15. WEAKLY CHAOTIC FMR.

Seemingly weak chaos realizes at  $h = 0.005$ . The Fig.10 shows evidence for (i) good correlation between the energy and dissipation (with  $E_0 = 0$  and  $\Gamma$  well related to actual friction coefficient  $\gamma$ ), and, at plot (D), (ii) rigid correlation between energy and average longitudinal component of magnetization,  $\langle S_{\parallel} \rangle$ . Here  $\langle \cdot \rangle$  denotes space-time averaging. Notice that in most part of film area  $S_{\parallel} = \langle S_0, S \rangle \approx S_y$ .

The latter correlation just gives the evidence that non-local energy contribution is relatively small. Indeed, because of relations

$$\|S_z\|^2 \approx \|S_x\|^2/p^2, \quad \langle S_x^2 \rangle + \langle S_z^2 \rangle \approx 2(1 - \langle S_{\parallel} \rangle),$$

where  $p$  is characteristic eccentricity,  $E_{loc}$  can be expressed as

$$E_{loc} \approx \left( H_0 + \frac{4\pi}{p^2 + 1} \right) (1 - \langle S_{\parallel} \rangle) \quad (8)$$

Hence, at  $E_{nonloc} \ll E_{loc}$  total excess energy also well reduces to  $\langle S_{\parallel} \rangle$ . If we equated  $p$  to small-amplitude uniform precession eccentricity given by Eq.5.10, then at  $H_0 = 3$  the Eq.8 would yield  $dE/d\langle S_{\parallel} \rangle \approx dE_{loc}/d\langle S_{\parallel} \rangle \approx -5$ . This value is lower by 10% than the slope ( $\approx -5.6$ ) at Fig.10.D. The difference can be explained if take into account that increase in spatial non-uniformity of precession result in decrease of its eccentricity.

Plot (G) in Fig.10 presents spectrum of power absorption (absolute value of Fourier transform of  $P(t)$ ). At  $M_s \approx 140$  Oe (as for YIG), the dimensionless frequency unit corresponds to  $\approx 390$  MHz, hence, the dominating frequency in  $P(t)$ 's spectrum is  $\approx 20$  MHz. Chaos in instant frequency of precession, as shown in plot (B), and thus in its phase is characterized by significantly wider frequency band (in part contained by plot (C) in Fig.9). Nevertheless, plot (F) in Fig10 visualizes anti-correlation between instant frequency and energy which corresponds to negative sign of non-isochronity (see Sec.5).

For fractal dimension (Sec.5.9) of these data it was found that  $d_{cor} < 3$  (see below). This implies that chaos is governed by three relevant variables only, and therefore chaotic attractor could be represented in 3-dimensional space. It seems doubtless that  $E$ ,  $P$  and  $\|S_x\|$  are relevant variables (due to Eq.5,  $P$  and  $\|S_x\|$  determine also the phase  $\phi$ ). Plot (C) in Fig.10 gives show of the attractor in these coordinates.

#### 6.16. ANALYSIS OF CORRELATION DIMENSION.

Let us discuss practical calculation of the correlation dimension,  $d_{cor}$  (Sec.5.9). At given correlation sum, one may estimate  $d_{cor}$  by two ways:

$$d_{cor} = \frac{d \ln \sigma(R)}{d \ln R} \quad \text{or} \quad d_{cor} = \frac{\ln[\sigma(R)/\Omega]}{\ln R} \quad (9)$$

The first of them may be called differential dimension while the second integral. Under formal limit  $N \rightarrow \infty$  these quantities are expected to coincide one with another. But real calculation needs in more than  $N^2$  operations, therefore  $N$  can not be as large as

wanted. Under realistic  $N$ , the differential estimate satisfactorily works at moderate values of  $R$  only,  $R_{\min} \ll R \ll R_{\max}$  (where  $R_{\min}$  is minimum of  $R_{ij}$ ). In opposite, the integral estimate better works at lower end of this interval.

Naturally, the integral estimate is less sensitive to finiteness of  $N$ , but instead it requires to know the coefficient  $\Omega$ . It is rather obvious that the best general assumption about  $\Omega$  is that it equals to volume of  $d_{cor}$ -dimensional unit-radius sphere, i.e.  $\Omega = \pi^{d_{cor}/2} / \Gamma(1 + d_{cor}/2)$ , where  $\Gamma$  means gamma-function. By special tests we verified that this recipe indeed constantly improves precision of  $d_{cor}$  estimates.

Notice that wide class of tests is presented by the Kaplan-Yorke chaotic system [1]. It is described by the set of difference (discrete time) equations:

$$X_j(t+1) = F(X_j(t)) \text{ , } j = 1 \dots n \text{ , } Y(t+1) = \alpha Y(t) + \sum_{j=1}^n f_j(X_j(t)) \text{ , } |\alpha| < 1 \text{ , } \quad (10)$$

where  $F(X)$  is some chaotic one-dimensional map (for instance, tent map,  $F(X) = 1 - |2X - 1|$ ), and  $f_j(X)$  are any smooth functions. Dependently on  $n$  and  $\alpha$ , fractal dimension of chaotic sequence  $Y(t)$  can be equated to arbitrary number (for example, for the tent map  $n = 2$  and  $\alpha = 1/16$  lead to  $d_{cor} = 2.5$  while  $n = 3$  and  $\alpha = 1/64$  to  $d_{cor} = 3.5$ ).

#### 6.17. FRACTAL DIMENSION OF CHAOTIC FMR.

Typical example of evaluation of  $d_{cor}$  is shown in Fig.11a (left plot). Here “log of Cell Size” in horizontal axis means  $\ln(R_{\max}/R)$  while vertical axis presents both the estimates (9). The dependencies of differential and integral dimensions on  $\ln(R_{\max}/R)$  are drawn by thin and fat lines, respectively.

We see that plateau in the first of them well coincides with the upper value of the second. From above mentioned tests, it is known that just this value should be taken as best estimate of  $d_{cor}$ , and that the coincidence signify good reliability of this estimate. In more complicated case when the plateau differs from upper (most right-hand) value of integral dimension, the latter must be preferred. But such the situation testifies that either the data (finite chaotic series) are not enough representative or they possess essential multifractality.

In case under consideration, fractal dimension of the power absorption time series under weakly chaotic FMR can be estimated as  $d_{cor} \approx 2.4$ .

To form better representative data, the time separation,  $\tau$ , in  $d$ -dimensional embedding points  $\{x(t_0+n\tau), x(t_0+n\tau+\tau), \dots, x(t_0+n\tau+d\tau)\}$  should be a few times shorter than characteristic correlation time of  $x(t)$ , while number of points must be sufficient for minimum “filling” of all of  $d$  dimensions, at least  $N \geq 2^d$ .

#### 6.18. CHAOTIC FMR IN DEFECTIVE FILM.

Real films always have more or less amount of defects. The right-hand plot in Fig.11a demonstrates static magnetization by tangential field in film with periodic lattice of defects (punctures) which touch about 10% of film area. Naturally, mean internal field,  $W_0$ , and thus characteristic precession frequencies are lowered by defects. But we found no qualitative difference between chaotic FMR in defective film and “good” film.

The top and left bottom plots in Fig.11b illustrate how the uniform component of spin precession behaves at small time scale (of order of  $1\text{ ns}$ ) and at moderate time scale (of order of  $0.1\text{ }\mu\text{s}$ ). On right hand, contour plot of spatial Fourier transform of  $S_{\perp x}$  shows that two groups of MSW modes form magnetization pattern, both belonging to the same frequency range around  $\omega_u$ , with the short-wave group induced by defect lattice. The levels for this plot were chosen specially to highlight short-wave modes. In fact, their contribution to energy is of order of a few percents.

#### 6.19. SYNCHRONIZATION OF CHAOTIC FMR.

In the work [4] synchronization of magnetic chaos under non-linear FMR in normally magnetized YIG film was experimentally realized. First, the signal,  $P_M(t)$ , related to power absorption was recorded into a memory. Characteristic frequencies of this signal were between 0.5 MHz and 10 MHz. The similar actual “slave” signal,  $P_S(t)$ , was compared with the recorded “master” signal, and the difference was directed, with some proportionality constant,  $K$ , to perturb the external magnetizing field,  $H_0 \rightarrow H_0 + K(P_M - P_S)$ . At suitable choice of  $K$ , after a transient time  $\sim 10\text{ }\mu\text{s}$ , excellent coincidence between  $P_S(t)$  and  $P_M(t)$  was observed.

The Fig.12 illustrates the attempt to numerically reproduce such the experiment but with tangentially magnetized film. The above mentioned defective film model is explored, at  $H_0 = 3$  and  $h = 0.005$ . The power absorption per unit volume,  $P(t)$ , is taken to serve as the control signal. The master signal to be addressed to the feedback,  $P_M(t)$ , either equals to  $P(t)$  or formed from it by slight time-smoothing (over  $5 \div 30$  periods of precession). Typical magnitude of chaotic  $P(t)$ ’s variations is  $\sim 5 \cdot 10^{-5}$ . The feedback

coefficient,  $K$ , is changed in the range between  $-30$  and  $-600$ .

Unfortunately,  $10\mu s$  is rather large time for our numerical simulations. Total duration of numerical runs was just about  $10\mu s$ . Best signs of synchronization were observed at  $K \sim 200$ . Hence, magnitude of the bias field modulation was  $\sim 0.01$ , i.e.  $\sim 1.5$  Oe in real units. For comparison, in [4] essentially smaller values  $\sim 0.1$  Oe were in action.

According to Fig.12, with no doubts synchronization takes place, but its quality is far from so excellent as reported in [4]. Possibly, this is due to wider frequency range of the control signal in our system, up to  $\sim 50$  MHz (see plot of  $P(t)$ 's spectra in Fig.12) and to not long enough duration of the numeric experiment.

### REFERENCES

1. A.J.Lichtenberg and M.A.Lieberman. Regular and stochastic motion. Springer-Verlag, 1988.
2. S.M.Rezende and F.M.de Aguiar. Proc. IEEE, 78 (1990) 893.
3. J.Beeker, F.Rodelsperger, Th.Weyrauch, H.Benner, W.Just and A.Cenys. Phys.Rev. E59 (1999) 1622.
4. D.W.Peterman, M.Ye and P.E.Wigen. Phys.Rev.Lett. 74 (1995) 1740.

### Conclusion

The above expounded material leads to conclusions as follow:

(i) Concepts, formulas and observations of linear theory of magnetostatic spin waves (MSW) in infinite films (Sections 2-4 of Part I, see arXiv preprint 1204.0200), as well as that of quasi-linear MSW theory (Sec.5 in the Part I), appear quite adequately useful for interpretation of numeric simulations of even non-linear and chaotic MSW even in small-size films;

(ii) Most effective way to MSW chaos is via parametric resonance and parametric non-linear transformations of MSW;

(iii) MSW chaos typically is determined by a few relevant variables only, - i.e. characterized by rather low fractal dimension, - and therefore seems allowing its control and more or less satisfactory synchronization.

The two last features will be further investigated in next Part III of this manuscript,



concentrating on not externally driven but auto-generated MSW chaos.

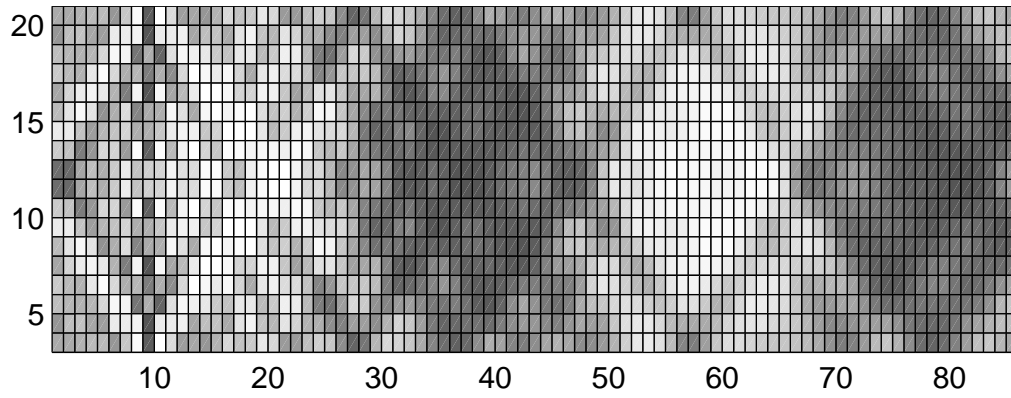


Fig.6a. Instant  $S_{\perp z}$ -pattern in small-area in-plane magnetized film under weak non-resonant excitation by wire positioned at  $x/D=9$ . Both external field and wire are parallel to  $y$ -axis. Parameters:  $H_0=3$ ,  $\gamma=0.003$ , exciting frequency  $\omega_e=7$ .

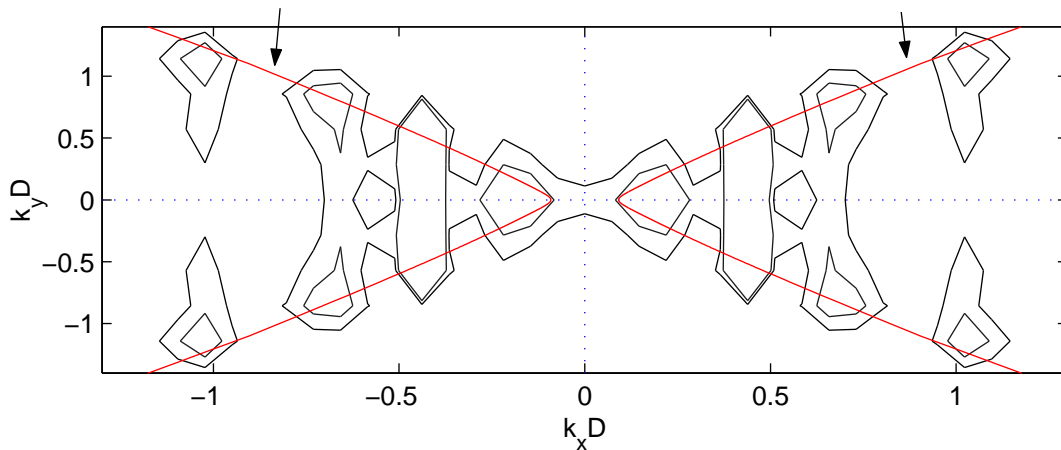
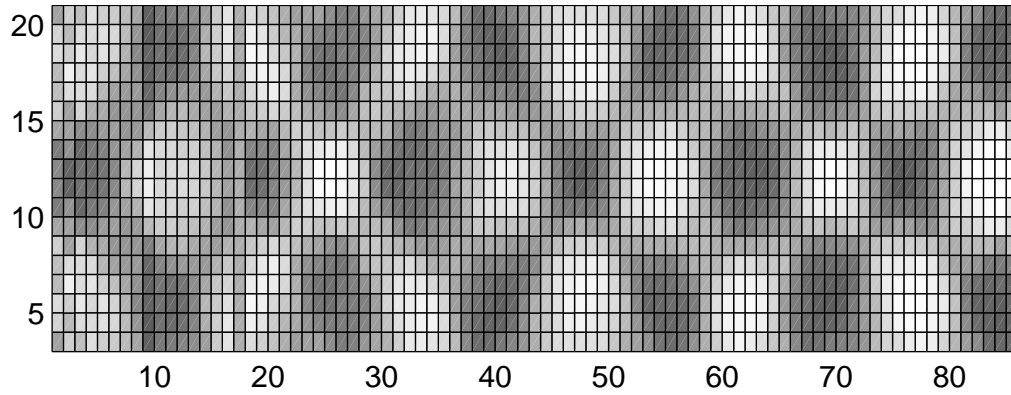


Fig.6b. (Top) The same as in Fig.6a but inductor is loop taking lines  $x/D=9$  and  $x/D=17$ . Both external field and loop are parallel to  $y$ -axis. Parameters:  $H_0=3$ ,  $\gamma=0.003$ ,  $\omega_e=7.3$ .  
(Bottom) Contour plot of spatial spectrum of  $S_{\perp z}$ -pattern. The curve marked by arrows is theoretical equi-frequency line  $\omega=\omega_e=7.3$  for surface waves (see Fig.4a).

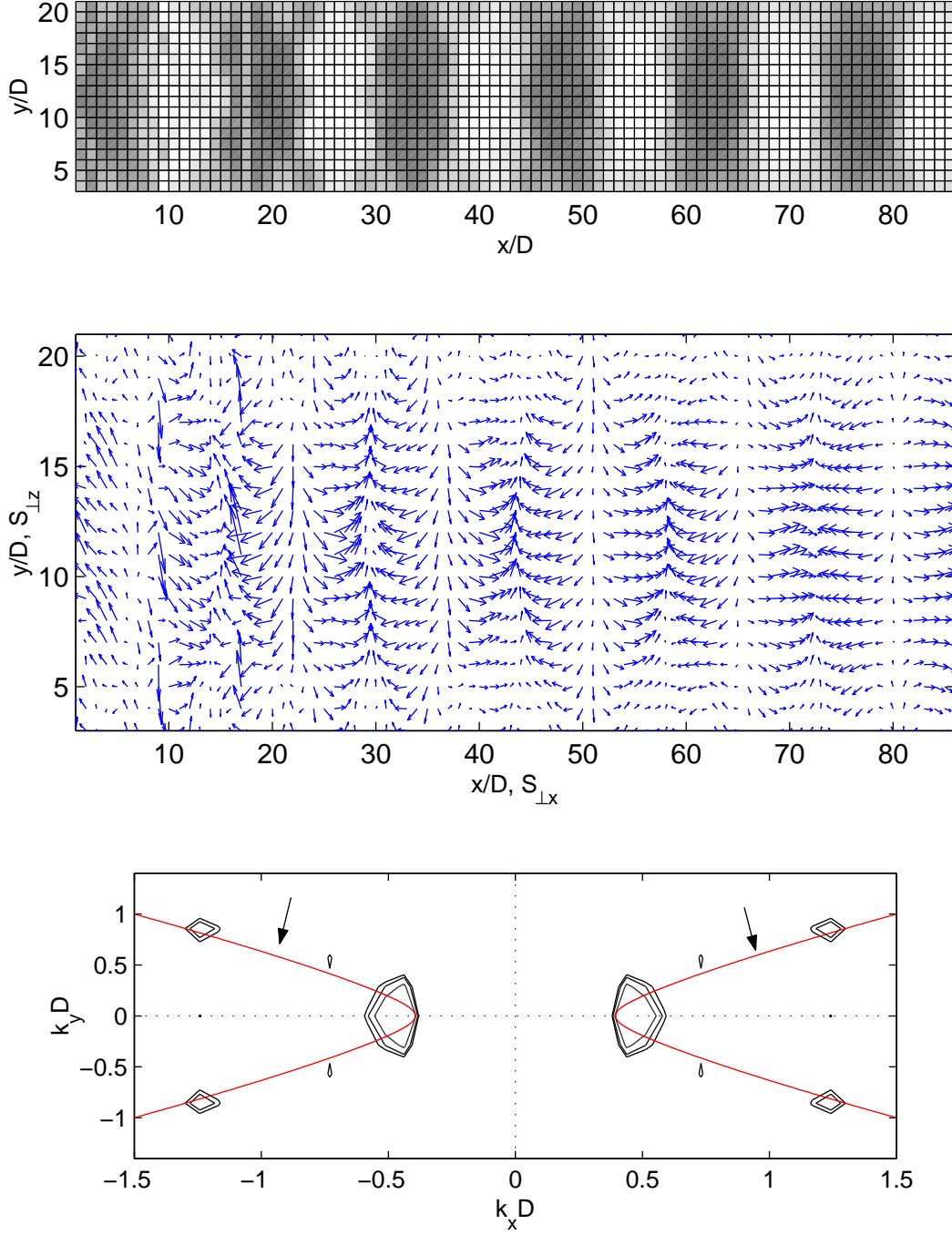


Fig.6c. (Top) Instant  $S_{\perp x}$  pattern under nearly resonant excitation by loop current with frequency  $\omega_e = 8.26 \approx \omega_{DE}(2\pi D/2l)$ ,  $l=8D$ . Other parameters as in Fig.6b.

(Middle) Corresponding instant distribution of the vector  $S_{\perp}$ .

(Bottom) Contour plot of spatial spectrum of  $S_{\perp z}$ . The curve marked by arrows is equi-frequency line corresponding to  $\omega = \omega_e$  (see Fig.4a).

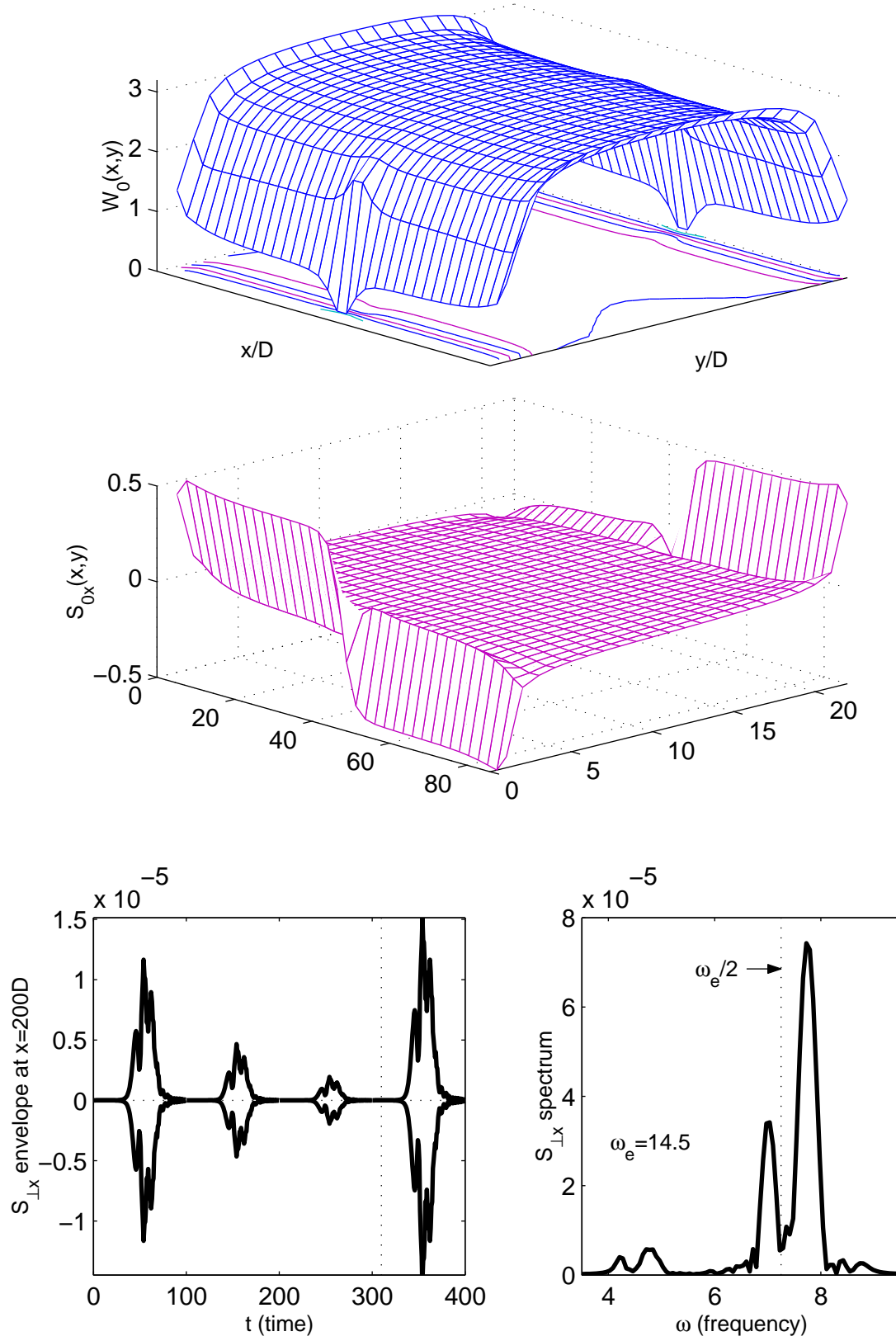


Fig.7. (Top & Middle) Internal field,  $W_0$ , and x-component of static magnetization,  $S_{0x}$ , in small-area film under external field  $H_0=3$  parallel to y-axis. (Bottom) Parametric subharmonics generation under excitation by weak loop induced field  $h_x=\pm 0.0002\sin(\omega_e t)$  applied to left edge, at  $H_0=3$ ,  $\gamma=0.0005$ ,  $\omega_e=14.5$ . Left: magnetization disturbance in the middle of film. Right: its spectrum occurs near  $\omega_e/2$ .

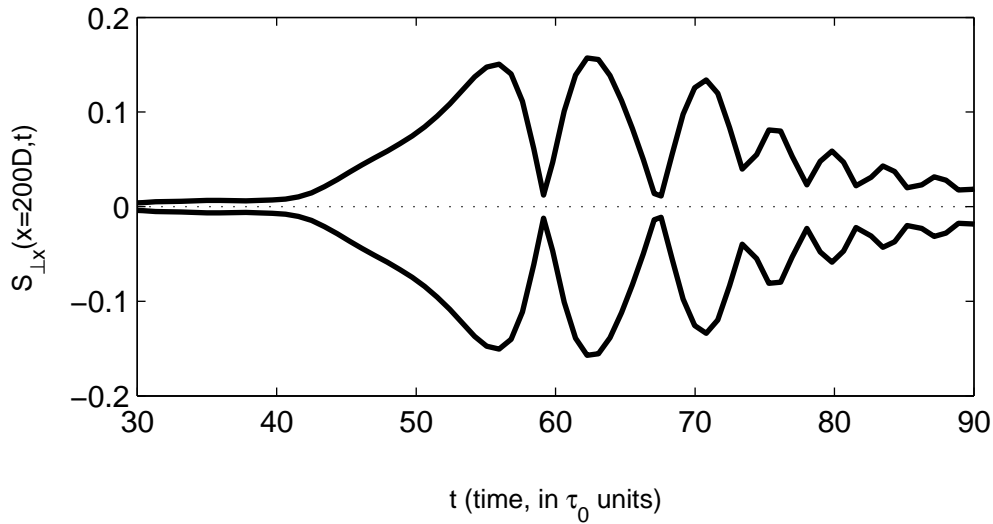


Fig.8a. Beginning of soliton formation under strong wire-induced field with  $h_x \sim 0.2 \sin(\omega_e t)$  applied to left edge, at  $H_0=3$ ,  $\gamma=0.0005$ ,  $\omega_e=7.5$ . The envelope of  $S_{\perp x}(x=200D, t)$  is shown.

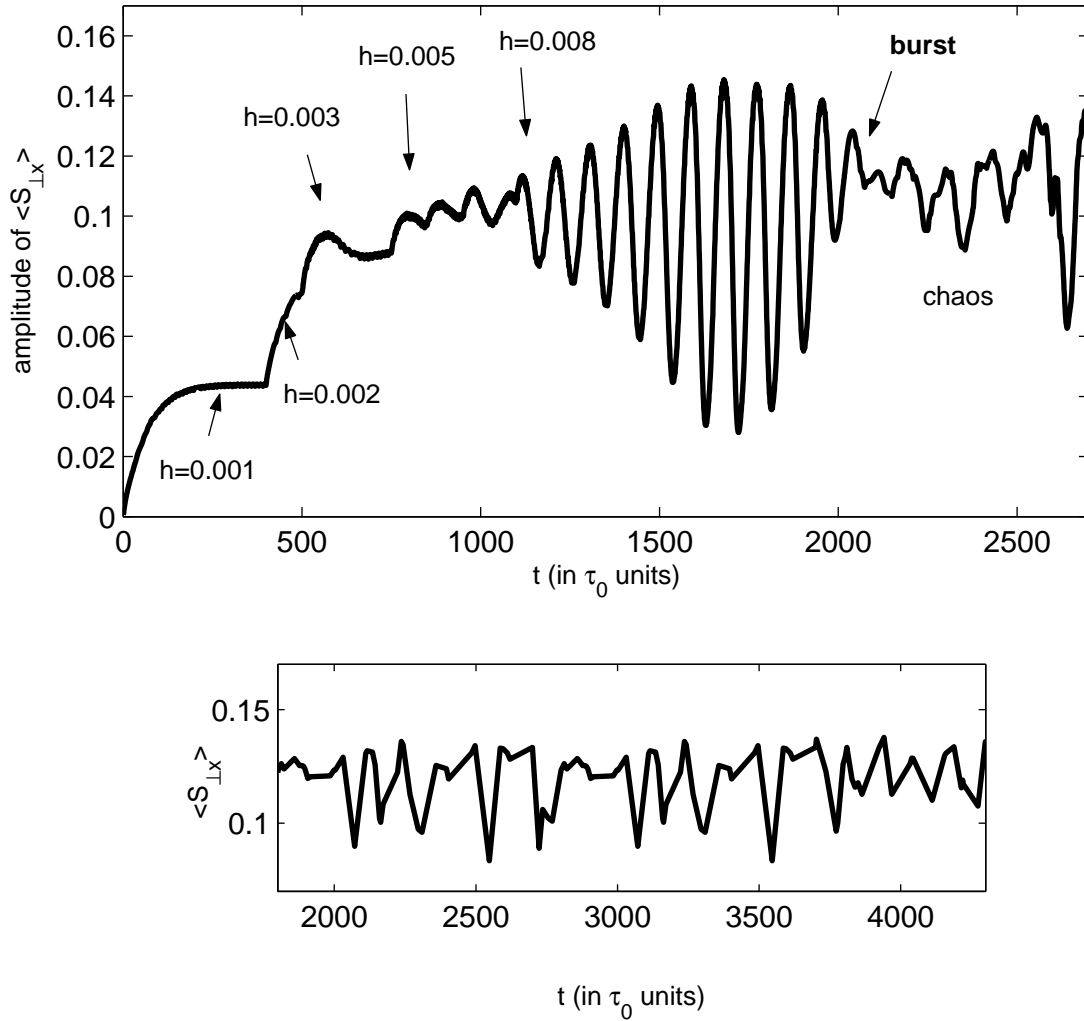


Fig.8b. Nearly resonant excitation of in-plane magnetized film by uniform radio-frequency field,  $h_x = h \sin(\omega_e t)$ , at  $H_0=3$ ,  $\gamma=0.0007$ ,  $\omega_e=6.785$ . (Top) Transition from stable FMR regime to chaos as the field,  $h$ , grows from 0.001 to 0.008. (Bottom) Chaotic oscillations of uniform magnetization component  $\langle S_{\perp x} \rangle = \int_V S_{\perp x}(r, t) dr / V_{21}$  in both plots its amplitude is shown.

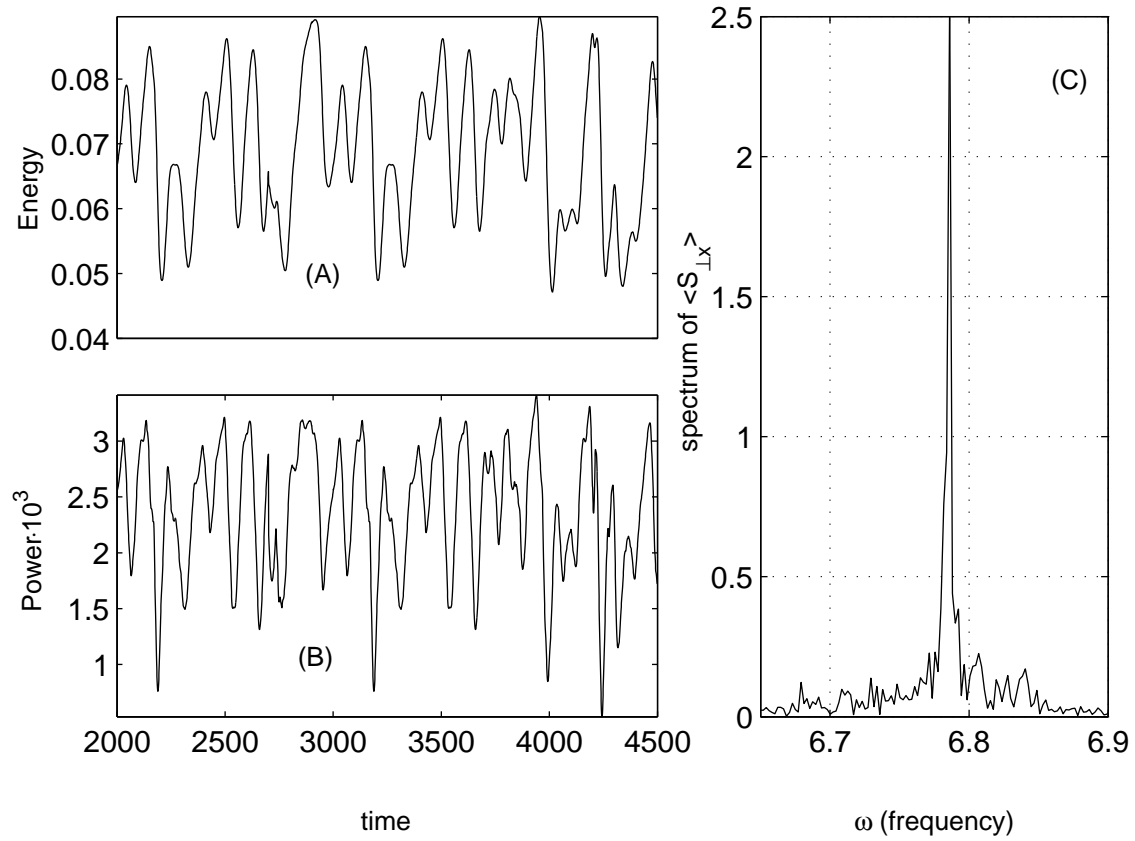


Fig.9. Chaotic ferromagnetic resonance of in-plane magnetized film excited by uniform radio-frequency field,  $h_x = 0.008 \sin(\omega_e t)$ , at  $H_0 = 3$ ,  $\gamma = 0.0007$ ,  $\omega_e = 6.785$ . (A) Excess energy per unit volume. (B) Power absorption per unit volume. (C) Spectrum of particular chaotic realization of  $\langle S_{\perp x} \rangle$ . (D) Instant  $S_{\perp x}$  pattern before transition to chaos. (E) Characteristic  $S_{\perp x}$  pattern at the moment of transition to chaos (marked "burst" in Fig.8b). The explosive birth of short magnetic waves and mirror symmetry violation are clearly seen.

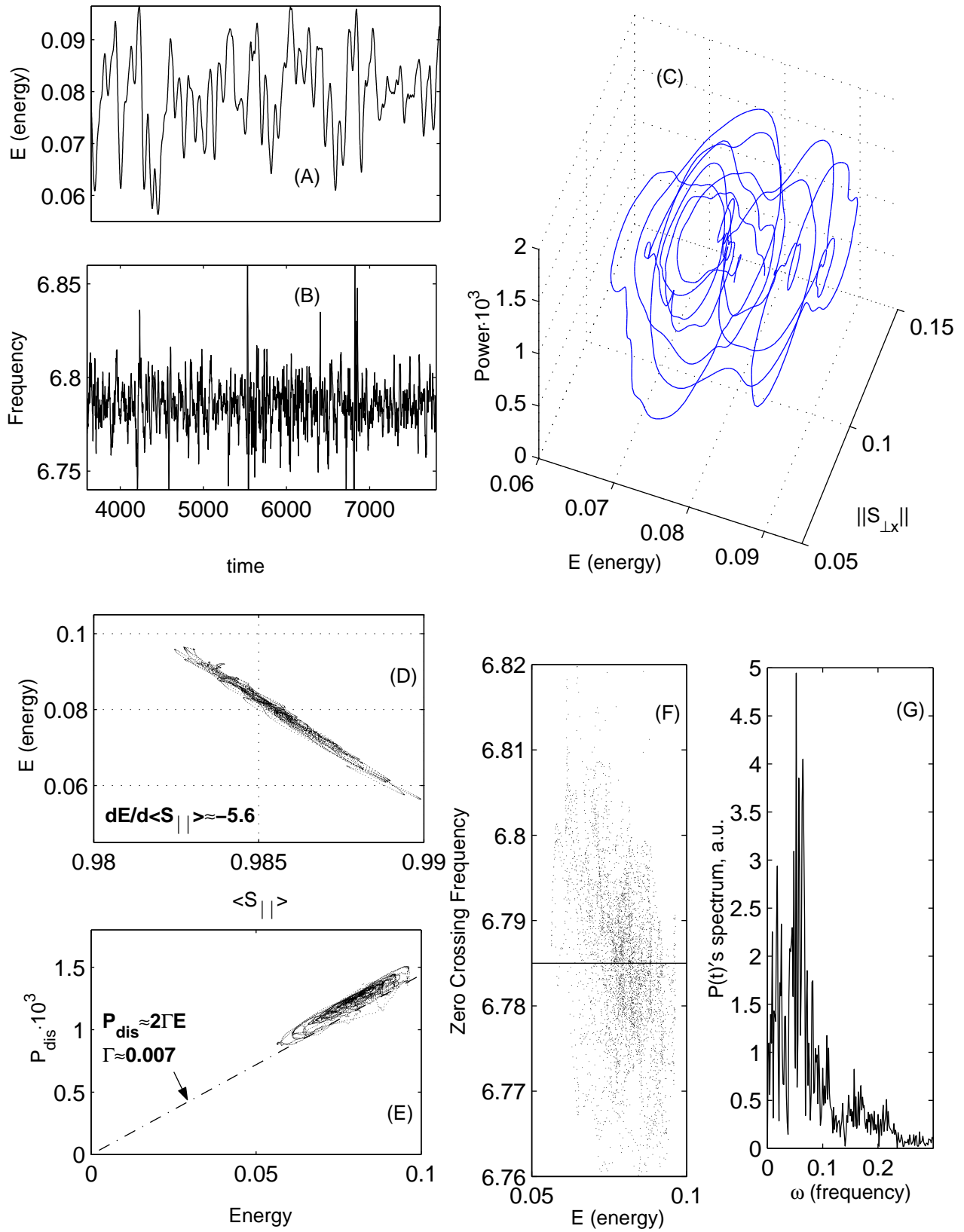


Fig.10. Chaotic FMR in uniform field,  $h_x = 0.005 \sin(\omega_e t)$ , at  $H_0 = 3$ ,  $\gamma = 0.0007$ ,  $\omega_e = 6.785$ .  
 (A) Excess energy. (B) Instant frequency of  $\langle S_{\perp x}(t) \rangle$  determined by its zero crossings.  
 (C) Fragment of chaotic attractor. (D) Correlation between energy,  $E$ , and  $\langle S_{\parallel} \rangle$ .  
 (E) Correlation between energy,  $E$ , and instant frequency. (F) Correlation between  
 dissipated power,  $P_{\text{dis}}$ , and energy. (G) Spectrum of power absorption.

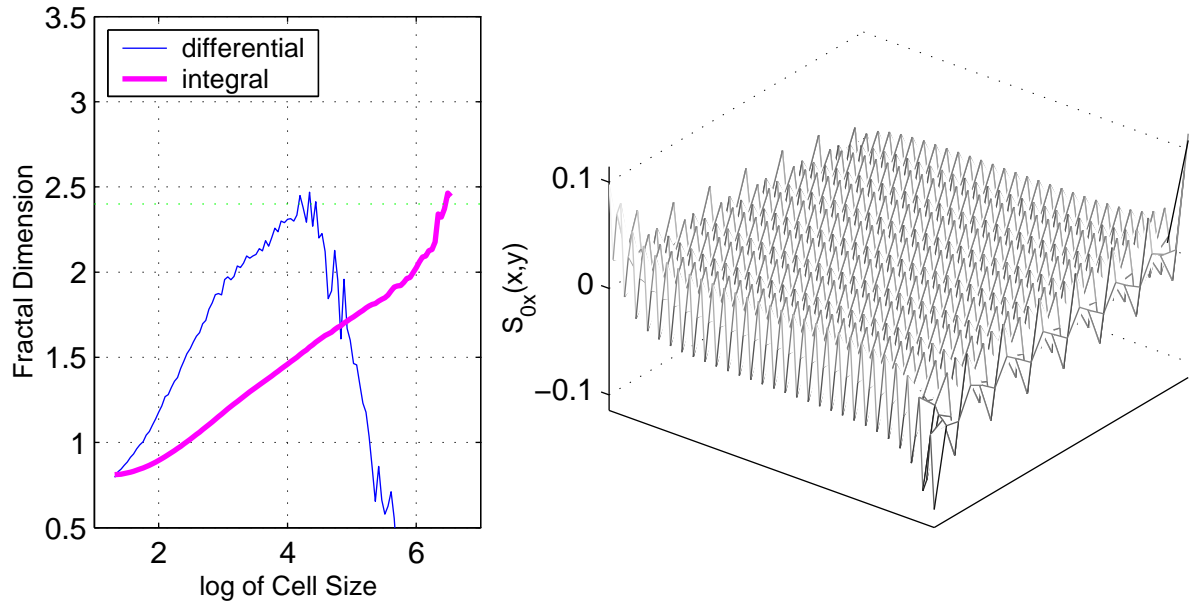


Fig.11a. Left: Fractal (correlation) dimension of absorbed power signal,  $P(t)$ , obtained by its embedding into 10-D space. The result is  $d_{\text{cor}} \approx 2.4$ . Right:  $S_{0x}$ -component of static magnetization in periodically punctured film.

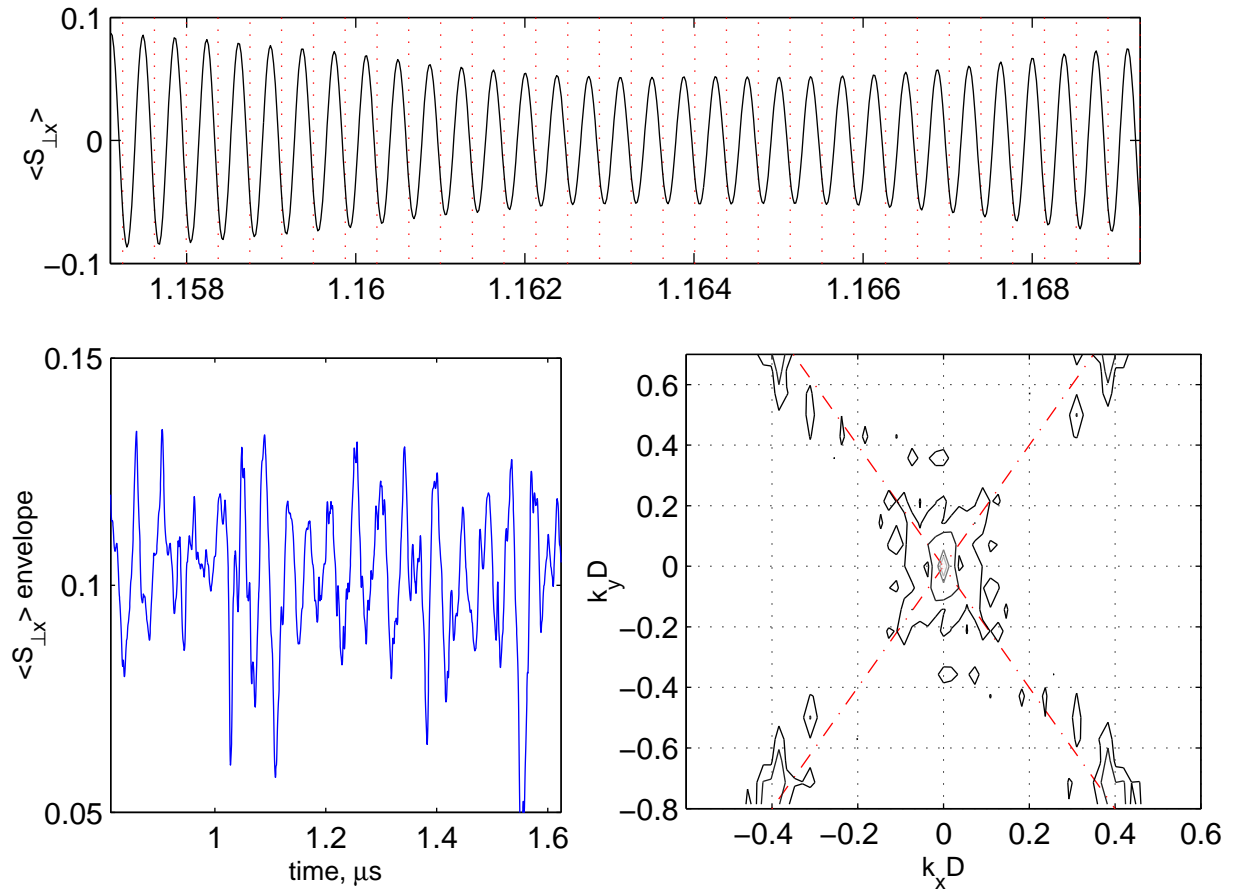


Fig.11b. (Top) Small piece of uniform component of magnetization excitation,  $\langle S_{\perp x} \rangle$  (dotted lines mark periods of exciting field). (Bottom left) Fragment of  $\langle S_{\perp x} \rangle$ 's envelope in chaotic FMR regime of in-plane magnetized film. (Bottom right) Contour plot of typical  $S_{\perp x}$ 's pattern. Dotted lines are theoretical equi-frequency lines for  $\omega = \omega_u$ , i.e.  $|k_y|/|k_x| = (4\pi/H_0)^{1/2}$ , at  $H_0 = 3$ .



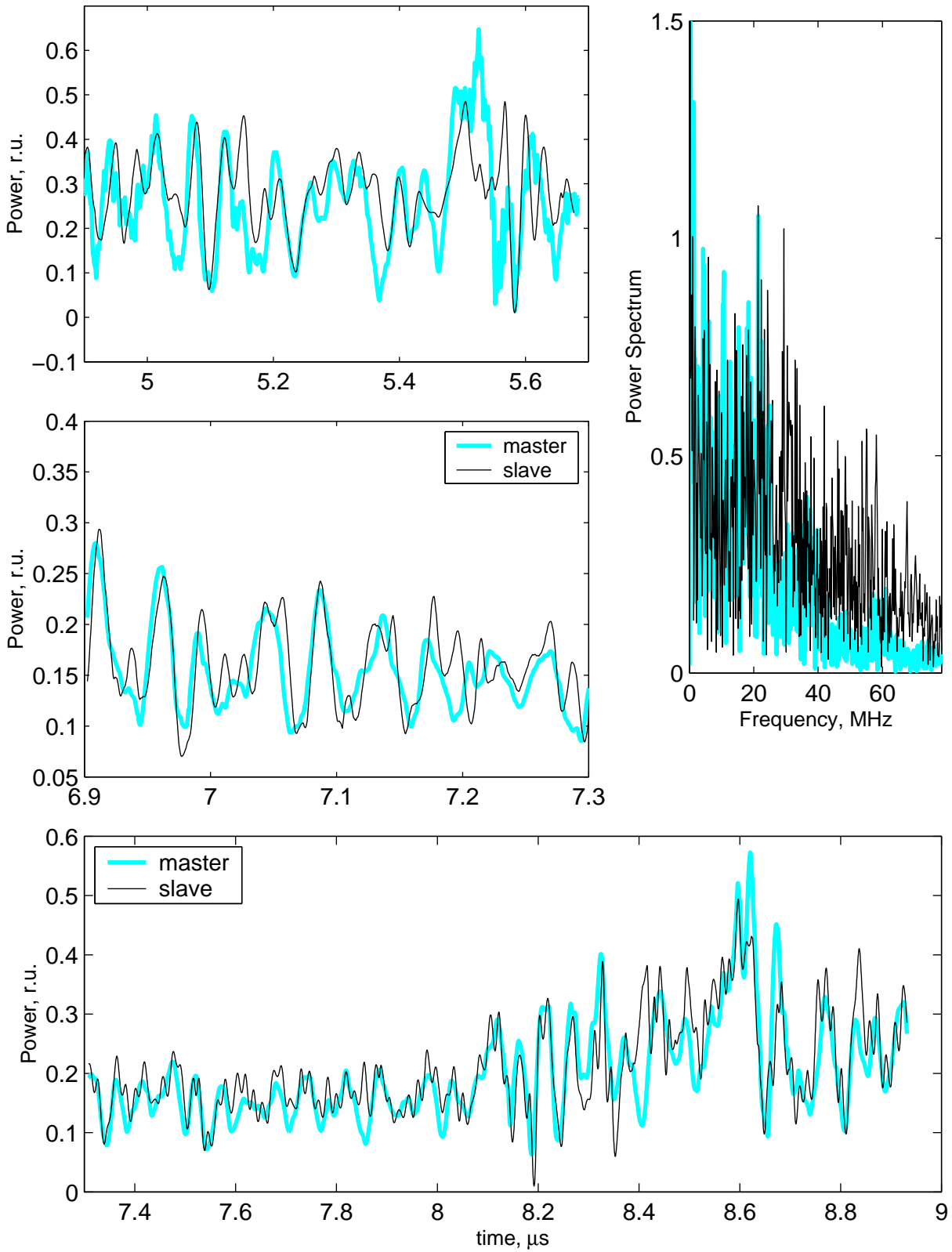


Fig.12. Synchronization of chaotic power absorption signal,  $P_{\text{slave}}(t)$ , at one film undergoing FMR by power signal,  $P_{\text{master}}(t)$ , from another film also subject to chaotic FMR. The films are identical, both periodically punctured, tangentially magnetized by field  $H_0=3M_s$  and excited by the same uniform field,  $h_x=0.005M_s \sin(\omega_e t)$ , whose frequency nearly equals to the uniform precession frequency,  $\omega_u \approx 5.65$ . For concreteness, in plots the value  $M_s=140$  Oe is substituted.